



AFRL-RY-WP-TR-2017-0155

**MEASUREMENT OF PHONON TRANSPORT IN
GaN-ON-SiC AND GaN-ON-DIAMOND HIGH ELECTRON
MOBILITY TRANSISTOR (HEMT) DEVICES**

Ronggui Yant

University of Colorado

**OCTOBER 2017
Final Report**

Approved for public release; distribution is unlimited.

See additional restrictions described on inside pages

STINFO COPY

**AIR FORCE RESEARCH LABORATORY
SENSORS DIRECTORATE
WRIGHT-PATTERSON AIR FORCE BASE, OH 45433-7320
AIR FORCE MATERIEL COMMAND
UNITED STATES AIR FORCE**

NOTICE AND SIGNATURE PAGE

Using Government drawings, specifications, or other data included in this document for any purpose other than Government procurement does not in any way obligate the U.S. Government. The fact that the Government formulated or supplied the drawings, specifications, or other data does not license the holder or any other person or corporation; or convey any rights or permission to manufacture, use, or sell any patented invention that may relate to them.

This report is the result of contracted fundamental research deemed exempt from public affairs security and policy review in accordance with SAF/AQR memorandum dated 10 Dec 08 and AFRL/CA policy clarification memorandum dated 16 Jan 09. This report is available to the general public, including foreign nationals.

Copies may be obtained from the Defense Technical Information Center (DTIC)
(<http://www.dtic.mil>).

AFRL-RY-WP-TR-2017-0155 HAS BEEN REVIEWED AND IS APPROVED FOR PUBLICATION
IN ACCORDANCE WITH ASSIGNED DISTRIBUTION STATEMENT.

BLEVINS.JOHN.D.1230263902
Digitally signed by
BLEVINS.JOHN.D.1230263902
DN: c=US, o=U.S. Government, ou=DoD,
ou=PKI, ou=USAF,
cn=BLEVINS.JOHN.D.1230263902
Date: 2017.09.18 15:11:55 -04'00'

*JOHN D. BLEVINS, Program Manager
Devices for Sensing Branch
Aerospace Component & Subsystems Division

DETTMER.ROSS.W.1076451806
Digitally signed by DETTMER.ROSS.W.1076451806
DN: c=US, o=U.S. Government, ou=DoD, ou=PKI,
ou=USAF, cn=DETTMER.ROSS.W.1076451806
Date: 2017.09.27 13:10:25 -04'00'

ROSS W. DETTMER, Chief
Devices for Sensing Branch
Aerospace Component & Subsystems Division

BEARD.TODD.W.1140628677
Digitally signed by
BEARD.TODD.W.1140628677
Date: 2017.10.12 14:03:22
-04'00'

TODD W. BEARD, Lt Col, USAF
Deputy
Aerospace Component & Subsystems Division
Sensors Directorate

This report is published in the interest of scientific and technical information exchange, and its publication does not constitute the Government's approval or disapproval of its ideas or findings.

*Disseminated copies will show “//Signature//” stamped or typed above the signature

REPORT DOCUMENTATION PAGE					<i>Form Approved OMB No. 0704-0188</i>	
The public reporting burden for this collection of information is estimated to average 1 hour per response, including the time for reviewing instructions, searching existing data sources, gathering and maintaining the data needed, and completing and reviewing the collection of information. Send comments regarding this burden estimate or any other aspect of this collection of information, including suggestions for reducing this burden, to Department of Defense, Washington Headquarters Services, Directorate for Information Operations and Reports (0704-0188), 1215 Jefferson Davis Highway, Suite 1204, Arlington, VA 22202-4302. Respondents should be aware that notwithstanding any other provision of law, no person shall be subject to any penalty for failing to comply with a collection of information if it does not display a currently valid OMB control number. PLEASE DO NOT RETURN YOUR FORM TO THE ABOVE ADDRESS.						
1. REPORT DATE (DD-MM-YY) October 2017		2. REPORT TYPE Final		3. DATES COVERED (From - To) 13 May 2015 – 13 May 2016		
4. TITLE AND SUBTITLE MEASUREMENT OF PHONON TRANSPORT IN GaN-ON-SiC And GaN-ON-DIAMOND HIGH ELECTRON MOBILITY TRANSISTOR (HEMT) DEVICES				5a. CONTRACT NUMBER FA8650-15-1-7524		
				5b. GRANT NUMBER		
				5c. PROGRAM ELEMENT NUMBER 61101E		
6. AUTHOR(S) Ronggui Yang				5d. PROJECT NUMBER 1000		
				5e. TASK NUMBER N/A		
				5f. WORK UNIT NUMBER Y14H		
7. PERFORMING ORGANIZATION NAME(S) AND ADDRESS(ES) University of Colorado 1111 Engineering Drive, Mechanical Engineering, 427 UCB Boulder, CO 80309				8. PERFORMING ORGANIZATION REPORT NUMBER		
9. SPONSORING/MONITORING AGENCY NAME(S) AND ADDRESS(ES) Air Force Research Laboratory Sensors Directorate Wright-Patterson Air Force Base, OH 45433-7320 Air Force Materiel Command United States Air Force				10. SPONSORING/MONITORING AGENCY ACRONYM(S) AFRL/Rydd		
				11. SPONSORING/MONITORING AGENCY REPORT NUMBER(S) AFRL-RY-WP-TR-2017-0155		
12. DISTRIBUTION/AVAILABILITY STATEMENT Approved for public release; distribution is unlimited.						
13. SUPPLEMENTARY NOTES This report is the result of contracted fundamental research deemed exempt from public affairs security and policy review in accordance with SAF/AQR memorandum dated 10 Dec 08 and AFRL/CA policy clarification memorandum dated 16 Jan 09. This material is based on research sponsored by Air Force Research laboratory (AFRL) and the Defense Advanced Research Agency (DARPA) under agreement number FA8650-15-1-7524. The U.S. Government is authorized to reproduce and distribute reprints for Governmental purposes notwithstanding any copyright notation herein. The views and conclusions contained herein are those of the authors and should not be interpreted as necessarily representing the official policies of endorsements, either expressed or implied, of Air Force Research Laboratory (AFRL) and the Defense Advanced Research Agency (DARPA) or the U.S. Government. Report contains color.						
14. ABSTRACT The objective of this project is to experimentally study the transient non-diffusive phonon transport in gallium nitride (GaN) based high electron mobility transistor (HEMT) devices. Using the ultrafast pump-probe thermoreflectance, we found that the measured thermal conductivity of the GaN substrate depends on the heating frequency and the metal thin film thickness. This novel phenomenon observed suggest that phonon transport in GaN would depend on both the structural and operating frequency.						
15. SUBJECT TERMS high electron mobility transistor, gallium nitride, silicon, carbide, phonon transport						
16. SECURITY CLASSIFICATION OF:			17. LIMITATION OF ABSTRACT: SAR	18. NUMBER OF PAGES 28	19a. NAME OF RESPONSIBLE PERSON (Monitor) John Blevins 19b. TELEPHONE NUMBER (Include Area Code) N/A	
a. REPORT Unclassified	b. ABSTRACT Unclassified	c. THIS PAGE Unclassified				

Table of Contents

Section	Page
List of Figures	ii
List of Tables	ii
1. SUMMARY	1
2. INTRODUCTION	2
3. FIRST PRINCIPLES CALCULATION OF PHONON MFP IN GaN, SiC, AND DIAMOND.....	4
3.1 Peierls-Boltzmann Transport Equation	4
3.2 Extracting Interatomic Force Constants from First-Principles	7
3.3 Results	8
4. FREQUENCY FILTERING EFFECT IN TIME-DOMAIN THERMOREFLECTANCE	12
4.1 Implementation of the TDTR Measurement	12
4.2 Frequency Filtering Effect of the Metal Thin Film in TDTR	14
4.3 Experimental Observation of the Frequency Filtering Effect	16
5. SUMMARY	20
6. REFERENCES	21
LIST OF ABBREVIATIONS, ACRONYMS, AND SYMBOLS	23

List of Figures

Figure	Page
Figure 1: Schematic of GaN HEMT Device Geometry	2
Figure 2: Crystal Structure of Diamond, w-GaN and 4H-SiC	4
Figure 3: Calculated Phonon Dispersion Relation of (a) Diamond, (b) w-GaN, and (c) 4H-SiC	9
Figure 4: Thermal Conductivity of (a) Diamond, (b) w-GaN, and (c) 4H-SiC, as a Function of Temperature	10
Figure 5: Cumulative Thermal Conductivity as a Function of Phonon Mean Free Path	11
Figure 6: Schematic of TDTR Measurement	13
Figure 7: Measured TDTR Temperature Response Ratio (circles) $-V_{in}/V_{out}$ of bulk GaN at Pump Modulation Frequencies of 2.03 MHz and 5.03 MHz, Coated with 101-nm-thick Al Transducer	13
Figure 8: Calibration Measurement of our TDTR System	14
Figure 9: (a) Modulated Pump Pulses in Time Domain and (b) Pump Pulses in Frequency Domain	14
Figure 10: Physical Picture of Frequency Filtering Effect of the Transducer Layer at different Heating Frequencies	16
Figure 11: (a) Temperature Dependent Thermal Conductivity of GaN and (b) Frequency and Temperature Dependent Thermal Conductivity of Sapphire	17
Figure 12: (a) Temperature Dependent Thermal Conductivity of GaN and (b) Frequency and Temperature Dependent Thermal Conductivity of Sapphire	18
Figure 13: Aluminum Thickness Dependent and Frequency Dependent Thermal Conductivity of GaN at 100 K	18
Figure 14: Temperature Dependent (a) Thermal Conductivity of Al and (b) Conductance of the Al/GaN Interface	19

List of Tables

Table	Page
Table 1. Lattice Constants of Diamond, w-GaN, and 4H-SiC	7

1. SUMMARY

In gallium nitride (GaN)-based high electron mobility transistor (HEMT) devices, the heat flux could reach a few kW/cm^2 and the heat dissipation has become a critical issue. Due to the nanometer length scale of the device layers and the high density of interfaces, non-diffusive heat conduction plays a critical role in thermal transport of GaN devices manifested as thermal conductivity and the interfacial thermal resistance of the device layers. Therefore, understanding the phonon transport physics and reducing the near-junction thermal resistance are of critical need for practitioners. This work uses both theoretical and experimental method to investigate the non-diffusive phonon transport. From density functional theory (DFT) based Boltzman transport equation (BTE), phonon mean free paths of GaN, silicon carbide (SiC), and diamond are predicted to span in a wide range, from dozens of nanometers to several microns. Such wide range of mean free path (MFP) indicates that the non-diffusive phonon transport would even be significant at room temperature. We then use an ultrafast pump-probe thermoreflectance measurement system to characterize the thermal conductivity of GaN layers, and we found that the measured thermal conductivity is related to the length scale of temperature gradient (heating frequency) and the thickness of the thin film heaters. Both our theoretical and experimental work suggest that the thermal dissipation would be much less efficient than the bulk case, due to the high frequency transient heat transport. This research suggests that the size effect of thermal conductivity in GaN devices is collectively determined by several characteristic lengths, and the previous knowledge of size effect is too simple to understand heat dissipation in practical HEMT devices.

2. INTRODUCTION

GaN-based HEMTs are promising for next generation radar applications due to their wide band gap, high electron velocity, and high breakdown field. However, due to the high power density in GaN HEMT devices, localized self-heating with a heat flux approaching tens of kW/cm^2 can be a critical issue. Figure 1 shows a state-of-the-art GaN HEMT device geometry, where AlGaIn/GaN layers are heteroepitaxially grown on non-GaN substrates, such as high thermal conductivity SiC ($\sim 400 \text{ W m}^{-1} \text{ K}^{-1}$) and chemical-vapor-deposited (CVD) diamond ($1000\text{-}2000 \text{ W m}^{-1} \text{ K}^{-1}$) substrates, due to the limited commercial availability of bulk GaN substrates. Due to the lattice mismatch between GaN and SiC/diamond, there is a transition/adhesion layer from a couple of microns to tens of nanometers (latest generations, usually proprietary) between GaN and high thermal conductivity SiC/diamond substrates. These transition/adhesion layers are usually amorphous materials with defects, such as AlGaIn, AlN, or SiN, which can be the most resistive thermal pathway in the device and thus offsetting the advantages of using high thermal conductivity substrates. A key research task in high power GaN HEMTs is to reduce the “near-junction” thermal resistance, as identified by the Defense Advanced Research Projects Agency (DARPA) Microsystems Technology Office (MTO).

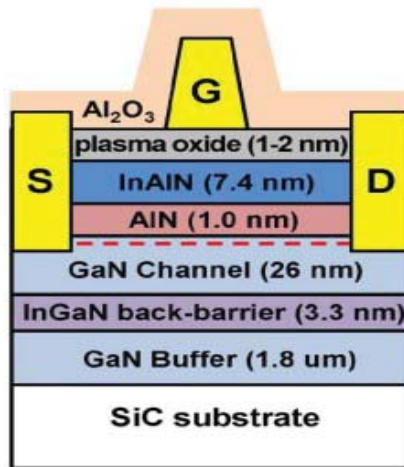


Figure 1: Schematic of GaN HEMT Device Geometry

To study the near-junction thermal transport and to reduce the near-junction thermal resistance of GaN devices, new strategies must be created to quantify contributions of each phonon modes to the thermal conductivity of the material stack in GaN-on-SiC and GaN-on-diamond devices. Measurement of phonon mean free path distributions in the materials at different temperature appears to be the most relevant yet most challenging task that can potentially bridge the rapid-growing fundamental understanding of phonon transport with practitioners' interest in device scaling.

As a statistical concept, the phonon MFP measures the average travelling distance between two consecutive phonon scattering events. Phonon MFP depends strongly upon the phonon modes and scattering details. The phonon scattering events include the 3-phonon and 4-phonon scattering due to the anharmonic nature of the interatomic potential, phonon-defects, phonon-

boundary/interface scattering. Contributions of phonons with different MFPs to heat transfer can be examined through the lattice thermal conductivity k along α direction predicted by the kinetic transport theory¹:

$$k_{\alpha\alpha} = \sum_{qs} C_{qs} v_{qs}^{\alpha} \Lambda_{qs}^{\alpha} \quad (1)$$

where $\mathbf{q}s$ represents the s -th phonon mode at \mathbf{q} in the first Brillouin zone, C_{qs} is the mode-specific heat capacity, v_{qs} is the group velocity, and the MFP Λ_{qs} for each phonon mode is the product of spectral phonon group velocity and relaxation time τ_{qs} , i.e., $\Lambda_{qs} = v_{qs} \tau_{qs}$. For a perfect bulk crystal, phonon MFP spans several orders of magnitude, from a few nanometers to tens of microns. The thermal conductivity can therefore be written as an integration over the entire phonon MFP:

$$k = \int_0^{\infty} \phi(\Lambda) d\Lambda \quad (2)$$

If the phonon mean free path is comparable or even smaller than the characteristic length of the device L_c , the thermal conductivity would reduce due to the suppressed phonon MFP:

$$k_A \sim \int_0^{L_c} \phi(\Lambda) d\Lambda \quad (3)$$

where k_A is the apparent thermal conductivity when the phonons transport is non-diffusive.

The wide range of phonon spectrum suggest that the thermal transport in HEMT nano-devices would significantly deviate from the diffusive transport in bulk limit due to the boundary scattering with the interface. Besides the boundary length of the GaN layer, there are also other length scales significantly affecting the thermal transport. For example, the length scale of the nano-sized heater²⁻³ and the length scale of temperature field⁴. In HEMT devices working in GHz range, the heating and thermal dissipation would be highly transient. We can therefore define the penetration depth as length scale of the temperature field:

$$d_p = \sqrt{k/\pi C f} \quad (4)$$

where f is the heating frequency. However, it is still not understood how different length scales simultaneously determine the phonon transport regime. Therefore, in this project, 1) we first use first principles-based calculations to predict the phonon mean free path spectrum and 2) we discovered frequency-filtering effect, a novel phenomenon that the thickness of the metal film and heating frequency simultaneously affect the measured apparent thermal conductivity.

3. FIRST PRINCIPLES CALCULATION OF PHONON MFP IN GaN, SiC AND DIAMOND

First principle-based methods for calculating the lattice thermal conductivity for a variety of bulk and nanostructured materials have been developed recently,⁵⁻⁸ where great agreement with the measured thermal conductivity values at different temperatures has been demonstrated. These calculations can differentiate the contributions to the total thermal conductivity of phonons with different wavelengths and different mean free paths. Here, we calculate the thermal conductivities and phonon mean free path distributions of diamond, w-GaN and 4H-SiC (see Figure 2) using the iterative solution of Peierls-Boltzmann transport equation.

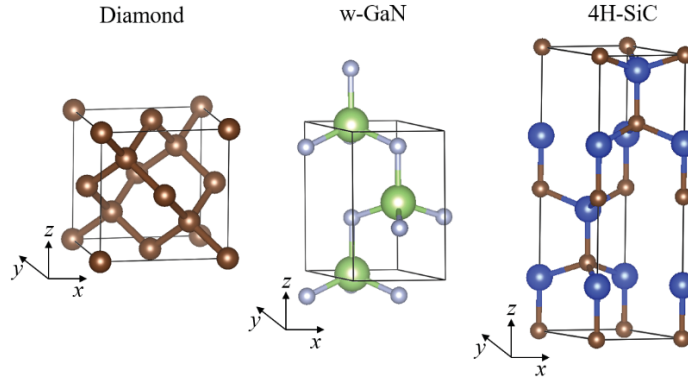


Figure 2: Crystal Structure of Diamond, w-GaN and 4H-SiC

3.1 Peierls-Boltzmann Transport Equation

To calculate the thermal conductivity along α ($= a, b, c$) direction, a small temperature gradient was applied along α direction, $\frac{\partial T}{\partial x^\alpha}$, to perturb the phonon population from the equilibrium Bose-Einstein distribution, n_{qs}^0 , to the non-equilibrium one, n_{qs} . When the steady state was achieved, the heat flux can be expressed as the summation of the contributions from all phonon modes through:

$$J^\alpha = \frac{1}{(2\pi)^3} \sum_s \int \hbar \omega_{qs} v_{qs}^\alpha n_{qs} d\mathbf{q} \quad (5)$$

where \hbar is the Planck constant, ω_{qs} is the frequency of phonon mode $\mathbf{q}s$. The phonon frequency ω_{qs} and v_{qs} can be obtained from the phonon dispersion of the crystal, while n_{qs} is determined by the Peierls-Boltzmann Transport Equation (PBTE). After J^α was calculated with the contributions from all phonon modes, the macroscopic thermal conductivity was then derived using the Fourier's law of heat conduction, $K_{\alpha\alpha} = -J^\alpha / (\frac{\partial T}{\partial x^\alpha})$. In order to evaluate the heat flux driven by the applied small temperature gradient, non-equilibrium phonon distribution of each phonon mode in Eq. (5) needs to be determined.

The phonon dispersion relation is related to the second-order harmonic force constants of the crystal, ϕ . With the harmonic force constants, the dynamical matrix \mathbf{D} can then be solved for phonon dispersion. The elements of \mathbf{D} are written as:

$$D_{\tau,\tau'}^{\alpha\beta}(\mathbf{q}) = \frac{1}{\sqrt{M_\tau M_{\tau'}}} \sum_{\mathbf{R}'} \phi_{0\tau,\mathbf{R}'\tau'}^{\alpha\beta} e^{i\mathbf{q}\cdot\mathbf{R}'} \quad (6)$$

where $\mathbf{R}\tau$ is the τ -th basis atom in the unit cell which is represented by the translation vectors \mathbf{R} , $M\tau$ is the atomic mass of the τ -th basis of the primitive cell. The phonon frequency, ω_{qs} , is the square root of the s -th eigenvalue of the dynamical matrix and the group velocity, v_{qs}^α , is calculated as $\partial\omega_{qs}/\partial q^\alpha$.

To determine the non-equilibrium phonon population distribution n_{qs} , it is convenient to express n_{qs} in the form of $n_{qs}^0 + n_{qs}^0(n_{qs}^0 + 1)\chi_{qs}^\alpha \frac{\partial T}{\partial x^\alpha}$ with deviation function χ_{qs}^α . The linearized PBTE, which describes the balance between phonon diffusion driven by the applied temperature gradient and phonon scattering, was then solved for the non-equilibrium phonon distribution function, or its equivalent χ_{qs} . In this work, we consider the three-phonon scattering and phonon-isotope scattering, and the corresponding PBTE can be expressed as⁵⁻⁶:

$$\begin{aligned} v_{qs}^\alpha \frac{\partial n_{qs}^0}{\partial T} = & \sum_{\mathbf{q}'s', \mathbf{q}''s''} \left[W_{qs, \mathbf{q}'s', \mathbf{q}''s''}^{\mathbf{q}''s''} \left(\chi_{\mathbf{q}''s''}^\alpha - \chi_{\mathbf{q}'s'}^\alpha - \chi_{qs}^\alpha \right) \right. \\ & + \frac{1}{2} W_{qs}^{\mathbf{q}'s', \mathbf{q}''s''} \left(\chi_{\mathbf{q}''s''}^\alpha + \chi_{\mathbf{q}'s'}^\alpha - \chi_{qs}^\alpha \right) \Big] \\ & + \sum_{\mathbf{q}'s'} \left[W_{qs, \mathbf{q}'s'}^{iso} \left(\chi_{\mathbf{q}'s'}^\alpha - \chi_{qs}^\alpha \right) \right] \end{aligned} \quad (7)$$

The first two terms on the right hand side of Eq. (4) are related to three-phonon scattering rates, and the third term is the scattering rates due to phonon-isotope scattering. Here, $W_{qs, \mathbf{q}'s', \mathbf{q}''s''}^{\mathbf{q}''s''}$ and $W_{qs}^{\mathbf{q}'s', \mathbf{q}''s''}$ are expressed as:

$$\begin{aligned} W_{qs, \mathbf{q}'s', \mathbf{q}''s''}^{\mathbf{q}''s''} = & 2\pi n_{qs}^0 n_{\mathbf{q}'s'}^0 \left(n_{\mathbf{q}''s''}^0 + 1 \right) |V_3(-\mathbf{q}s, -\mathbf{q}'s', \mathbf{q}''s'')|^2 \\ & \times \delta(\omega_{qs} + \omega_{\mathbf{q}'s'} - \omega_{\mathbf{q}''s''}) \delta(\mathbf{q} + \mathbf{q}' - \mathbf{q}'' + \mathbf{G}) \end{aligned} \quad (8)$$

$$\begin{aligned} W_{qs}^{\mathbf{q}'s', \mathbf{q}''s''} = & 2\pi n_{qs}^0 \left(n_{\mathbf{q}'s'}^0 + 1 \right) \left(n_{\mathbf{q}''s''}^0 + 1 \right) |V_3(-\mathbf{q}s, \mathbf{q}'s', \mathbf{q}''s'')|^2 \\ & \times \delta(\omega_{qs} - \omega_{\mathbf{q}'s'} - \omega_{\mathbf{q}''s''}) \delta(\mathbf{q} - \mathbf{q}' - \mathbf{q}'' + \mathbf{G}) \end{aligned} \quad (9)$$

where the δ function and the Δ function denotes the energy conservation condition $\omega_{qs} \pm \omega_{\mathbf{q}'s'} - \omega_{\mathbf{q}''s''} = 0$ and the momentum conservation condition $\mathbf{q} \pm \mathbf{q}' - \mathbf{q}'' + \mathbf{G} = \mathbf{0}$ for the three-phonon scattering process. The + and - signs represent the annihilation and decay processes, respectively.

The \mathbf{G} vector represents a reciprocal vector. The scattering is normal process when $\mathbf{G} = \mathbf{0}$, while it is Umklapp process when $\mathbf{G} \neq \mathbf{0}$. The three-phonon scattering matrix V_3 is written as:

$$V_3(\mathbf{q}s, \mathbf{q}'s', \mathbf{q}''s'') = \left(\frac{\hbar}{8N_0\omega_{\mathbf{q}s}\omega_{\mathbf{q}'s'}\omega_{\mathbf{q}''s''}} \right)^{\frac{1}{2}} \sum_{\tau} \sum_{\mathbf{R}'\tau'} \sum_{\mathbf{R}''\tau''} \sum_{\alpha\beta\gamma} \psi_{0\tau, \mathbf{R}'\tau', \mathbf{R}''\tau''}^{\alpha\beta\gamma} \\ \times \exp(i\mathbf{q}' \cdot \mathbf{R}' + i\mathbf{q}'' \cdot \mathbf{R}'') \frac{\varepsilon_{\mathbf{q}s}^{\tau\alpha} \varepsilon_{\mathbf{q}'s'}^{\tau'\beta} \varepsilon_{\mathbf{q}''s''}^{\tau''\gamma}}{\sqrt{M_{\tau}M_{\tau'}M_{\tau''}}} \quad (10)$$

where ε is the eigenvector of the dynamical matrix.

The isotope scattering matrix $W_{\mathbf{q}s, \mathbf{q}'s'}^{iso}$ is written as:

$$W_{\mathbf{q}s, \mathbf{q}'s'}^{iso} = \frac{\pi}{2} \omega_{\mathbf{q}s} \omega_{\mathbf{q}'s'} n_{\mathbf{q}s}^0 (n_{\mathbf{q}'s'}^0 + 1) \sum_{\tau} g_{\tau} \left| \sum_{\alpha} (\varepsilon_{\mathbf{q}s}^{\tau\alpha})^* \varepsilon_{\mathbf{q}'s'}^{\tau\alpha} \right|^2 \delta(\omega_{\mathbf{q}s} - \omega_{\mathbf{q}'s'}) \quad (11)$$

where g_{τ} is the mass variance parameter for the basis atom τ . The mass variance parameter is related to the concentration, c_i , and the mass, M_i , of the i -th constituent isotopes,

$$g = \frac{\sum_i c_i M_i^2 - (\sum_i c_i M_i)^2}{(\sum_i c_i M_i)^2} \quad (12)$$

In order to sample the reciprocal space for phonon scattering, and thermal conductivity calculations, Eq. (2), we discrete the first Brillouin zone into $N_1 \times N_2 \times N_3$ Γ -centered \mathbf{q} -points. The grid points are located at $\mathbf{q} = \frac{m}{N_1} \mathbf{b}_1 + \frac{n}{N_2} \mathbf{b}_2 + \frac{l}{N_3} \mathbf{b}_3$ where \mathbf{b}_1 , \mathbf{b}_2 , and \mathbf{b}_3 are reciprocal primitive lattice vectors, and m , n and l are integers. The delta function for the energy conservation condition in Eq. (5) and Eq. (6) is evaluated by the Gaussian function with an adaptive broadening parameter related to the local group velocity.¹⁰ The set of linear equations Eq. (7), with respect to $\chi_{\mathbf{q}s}^{\alpha}$, can be self-consistently solved through the iterative method. Here we employ the bi-conjugate gradient stabilized method,¹¹ a variant of the conjugate gradient algorithm, to iteratively solve Eq. (7). After $\chi_{\mathbf{q}s}^{\alpha}$ is calculated, the thermal conductivity can be expressed as

$$k_{\alpha\alpha} = \frac{1}{N_0\Omega} \sum_{\mathbf{q}s} \hbar \omega_{\mathbf{q}s} v_{\mathbf{q}s}^{\alpha} n_{\mathbf{q}s}^0 (n_{\mathbf{q}s}^0 + 1) \chi_{\mathbf{q}s}^{\alpha} \quad (13)$$

To quantify the importance that the temperature gradient collective scattering behavior of all the phonon modes plays on anisotropic phonon transport, we rewrite Eq. (10) into the form of Eq. (1) to defining the phonon MFP in the iterative approach, which reads as

$$\tilde{\tau}_{qs}^{\alpha} = (k_B T^2 / \hbar) \cdot (F_{qs}^{\alpha} / \omega_{qs}) \quad (14)$$

where k_B is the Boltzmann constant.

3.2 Extracting Interatomic Force Constants from First-Principles

All first-principles calculations are performed using the Quantum-Espresso package¹² with norm-conserving pseudopotential and the local-density approximation functional. The kinetic-energy cut-off for the plane-wave basis is set at 80 Ry. $12 \times 12 \times 12$, $6 \times 6 \times 6$ and $8 \times 8 \times 4$ k -meshes are used to sample electronic states in the reciprocal space of diamond, w-GaN and 4H-SiC, respectively. The choice of the energy cutoff and k -mesh ensures that the energy change is smaller than 1 meV/atom when refining these two parameters. The lattice structures are relaxed using the conjugated gradient method to minimize the energy of the crystal, and optimized lattice constants are summarized in Table 1, which are close to the values from experimental measurements.¹³⁻¹⁵

Table 1. Lattice Constants of Diamond, w-GaN, and 4H-SiC

Materials	a (nm)		c (nm)	
	DFT	Exp.	DFT	Exp.
Diamond	0.3527	0.3567 ¹³		
w-GaN	0.3160	0.3190 ¹⁵	0.5153	0.5189 ¹⁵
4H-SiC	0.3068	0.3073 ¹⁴	1.0045	1.0053 ¹⁴

To calculate the lattice thermal conductivity and phonon mean free path, both the second-order harmonic and third-order anharmonic interatomic force constants of each material are required. We use the density-functional perturbation theory (DFPT) approach¹⁶ to calculate the dynamical matrices of the phonon modes on the $6 \times 6 \times 6$ q -meshes for diamond, w-GaN and 4H-SiC. With the dynamical matrices, the harmonic force constants are calculated through the Fourier-transform of the obtained dynamical matrices. Both the DFPT and Fourier-transform are implemented in Quantum-Espresso.

For the third-order anharmonic force constants, the supercell scheme with a size of $4 \times 4 \times 4$, $3 \times 3 \times 3$ and $3 \times 3 \times 1$ primitive cells of diamond, w-GaN and 4H-SiC is employed. We displace two atoms in a supercell by $\Delta = 0.01$ Å away from their equilibrium position along $\pm x$, $\pm y$ and $\pm z$ directions simultaneously, and then record the forces, F , of all atoms in the supercell. With the recorded force information on all atoms in the supercell, the third-order force constants are calculated using the finite-difference scheme,¹⁷ which are expressed as

$$\psi_{0\tau, R'\tau', R''\tau''}^{\alpha\beta\gamma} = -\frac{1}{4\Delta^2} \left[F_{R''\tau''}^{\gamma} (u_{R\tau}^{\alpha} = \Delta, u_{R'\tau'}^{\beta} = \Delta) - F_{R''\tau''}^{\gamma} (u_{R\tau}^{\alpha} = \Delta, u_{R'\tau'}^{\beta} = -\Delta) - F_{R''\tau''}^{\gamma} (u_{R\tau}^{\alpha} = -\Delta, u_{R'\tau'}^{\beta} = \Delta) + F_{R''\tau''}^{\gamma} (u_{R\tau}^{\alpha} = -\Delta, u_{R'\tau'}^{\beta} = -\Delta) \right], \quad (15)$$

where u is the atom displacement from equilibrium position. The Lagrange multipliers approach¹⁸ is employed to enforce translational invariance for the third-order force constants, without which the long-wavelength phonons are likely to be more severely scattered and thus

underestimate the thermal conductivity. The cutoffs for the third-order anharmonic interaction are chosen to the third nearest neighbors.

3.3 Results

Figure 3 shows the calculated phonon dispersion curves for diamond, w-GaN and 4H-SiC. We also plot the phonon dispersion measured by neutron scattering experiments. The good agreement with both the measurements¹⁹⁻²¹ validates the interatomic force constants from our first-principles calculations.

The calculated temperature-dependent thermal conductivity of silicon and sapphire is presented in Figure 4, as well as experimental data for both silicon²² and sapphire²³. Our calculations are close to these previous works.

The accumulative thermal conductivity gives the contribution from the phonons with MFP smaller than Λ to the total thermal conductivity. By summing up the thermal conductivity of phonon modes with MFPs in that range, the accumulative thermal conductivity can be determined.

Figure 5 shows the differential and cumulative thermal conductivity of diamond, w-GaN and 4H-SiC from first-principles calculations. It is found that the phonons with MFP larger than 1 μm in all materials studied contribute to more than 50% of the total thermal conductivity. Since the thickness of GaN thin film is around 800 nm in HEMT devices, the long-MFP phonons should behave quite different from the prediction from the Fourier's law and we have to consider how the ballistic transport affects the heat conduction in thin films as well as phonon transmission across the interfaces.

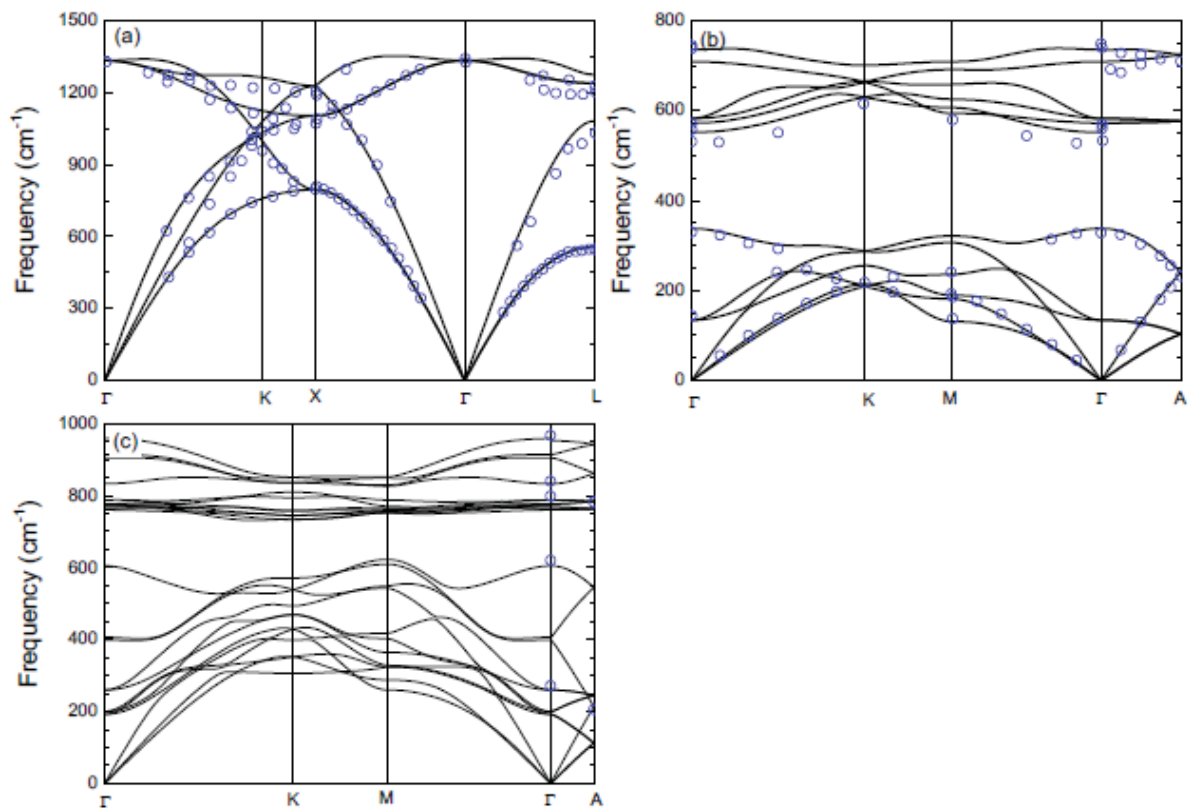


Figure 3: Calculated Phonon Dispersion Relation of (a) Diamond, (b) w-GaN, and (c) 4H-SiC

The blue dots in (a-c) represent the measured phonon dispersion of diamond¹⁹, w-GaN²¹, and 4H-SiC.²⁰

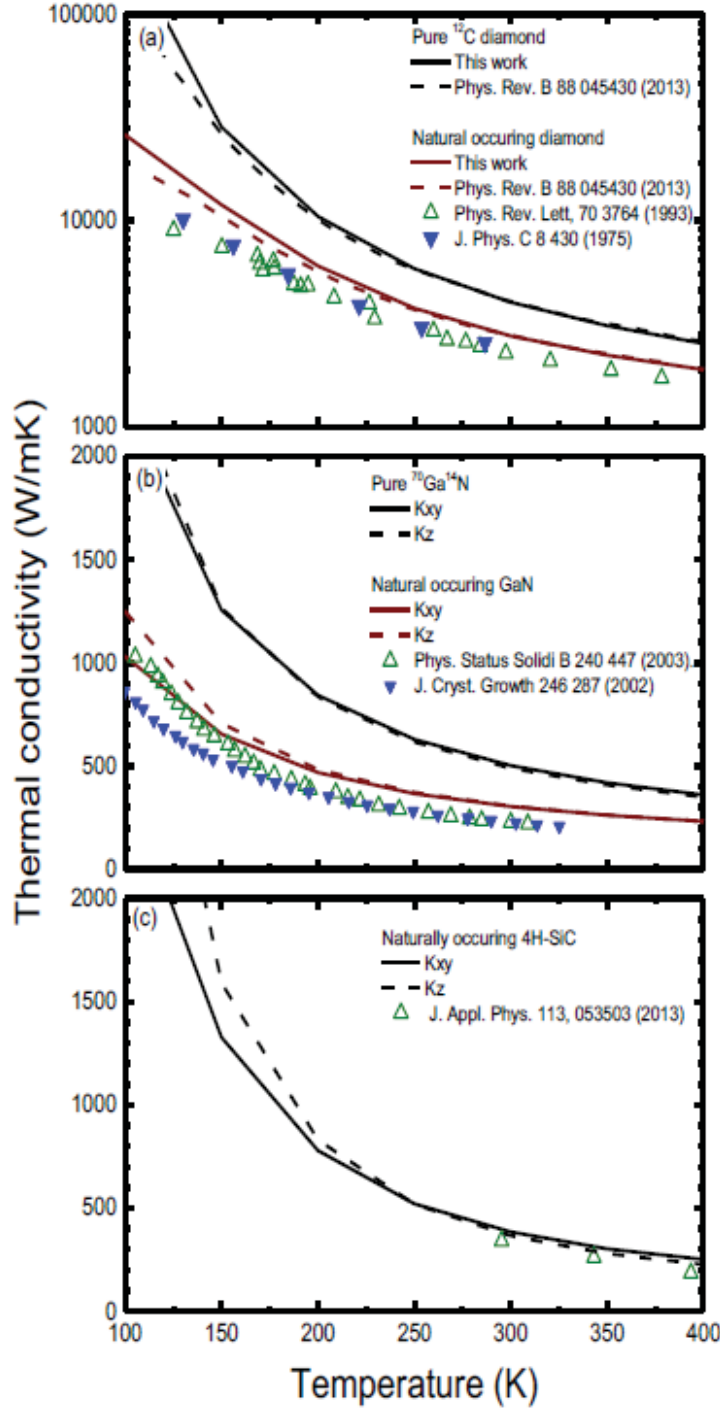


Figure 4: Thermal Conductivity of (a) Diamond, (b) w-GaN, and (c) 4H-SiC, as a Function of Temperature

The dash lines in (a) represent the calculated thermal conductivity of diamond using the first-principles based PBTE method²², while the green²³ and blue²⁴ dots are the measured thermal conductivity of diamond. The green²⁵ and blue²⁶ dots in (b) show the experimentally measured thermal conductivity for w-GaN. The dots in (c) represent the measured thermal conductivity of 4H-SiC.²⁷

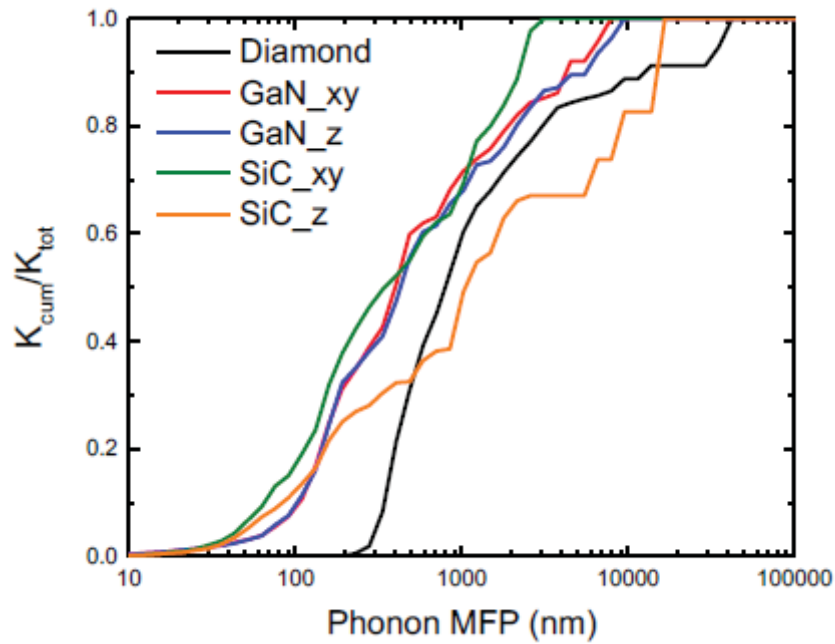


Figure 5: Cumulative Thermal Conductivity as a Function of Phonon Mean Free Path

4. FREQUENCY FILTERING EFFECT IN TIME-DOMAIN THERMOREFLECTANCE

Size effect in thermal conductivity has been intensively studied in the past two decades to understand the nanoscale thermal transport. For example, the thickness of GaN layer,²⁸ size of the heater,^{2-3, 29} and thermal penetration length (modulation frequency).³⁰⁻³¹ However, the size effect of thermal conductivity as a function a single length scale is over simplified for thermal transport in HEMT devices, because more than one characteristic lengths in HEMT devices together determines the phonon transport physics. To understand how different length scales simultaneously affect the apparent thermal conductivity, we simply the multi-layered HEMT device to a two-layer system with Al thin film deposited on GaN substrate. The Al thin film serves as the heater by absorbing the pump laser to create a periodic heating. Such simplification reduces the number of characteristic lengths to only two: the thermal penetration depth and the thickness of the Al thin film. We then use the time-domain thermoreflectance (TDTR) technique to optically measure the thermal conductivity of GaN in the Al/GaN sample. By varying the heating frequency and the thickness of the Al thin film, the measured apparent thermal conductivity is changed. We explain this novel phenomenon as the frequency filtering effect of the Al thin film. This work is the first observation on how different feature size simultaneously determine the phonon transport regime.

4.1 Implementation of the TDTR Measurement

Time-domain thermoreflectance measurement is an optical experiment to characterize thermal properties of materials. Figure 6 shows the experimental system implemented in our lab. A Ti-sapphire oscillator is used as the light source with wavelength centered at around 800 nm and a repetition rate of 80 MHz. The laser output is split into pump beam for heating and probe beam for sensing. Before focused onto the sample, the pump beam is modulated by an electro-optic modulator (EOM) at a frequency from a few kHz to a few MHz. The pump beam is then absorbed by the transducer layer (a metal thin film, usually 100 nm Al) deposited on the substrate, creating a periodic heating. The transducer serves as the sensor at the same time, because the reflectance change is proportional to the surface temperature rise. To monitor the surface temperature change, we use another delayed probe beam. The probe beam passes through a mechanical delay stage such that the temperature responses are detected with a delay time (≤ 8 ns in our lab) after the sample is heated by the pump pulse using a photodetector. The signal from thermoreflectance change is then extracted by the lock-in amplifier. To separate the probe beam which contains the reflectance change signal from the pump beam, we vertically separate the pump and the probe beam, and use an iris to block the reflected pump beam. Figure 7 shows an example of TDTR signal obtained on an Al/GaN sample. The thermal transport properties can be then extracted by fitting the signal with the heat conduction model.

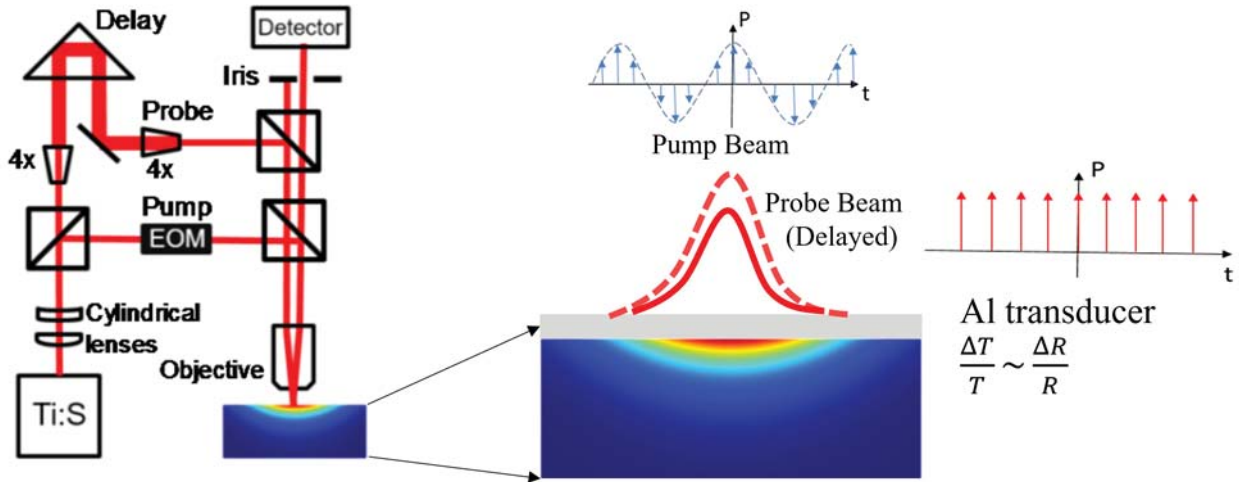


Figure 6: Schematic of TDTR Measurement

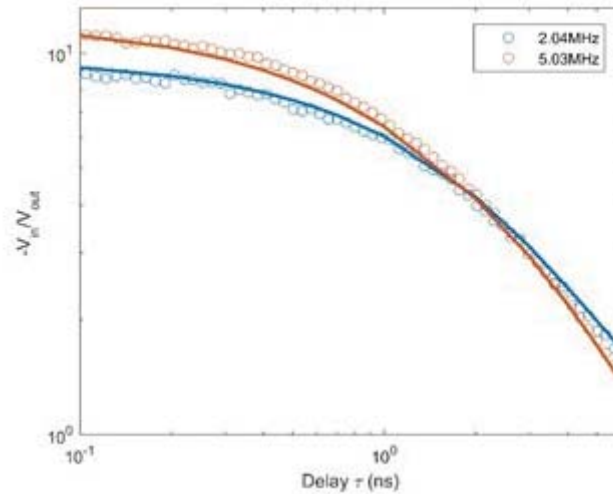


Figure 7: Measured TDTR Temperature Response Ratio (circles) $-V_{in}/V_{out}$ of bulk GaN at Pump Modulation Frequencies of 2.03 MHz and 5.03 MHz, Coated with 101-nm-thick Al Transducer

The color lines are predicted by a theoretical heat transfer model with thermal conductivity $k_{GaN} = 190 \text{ W/mK}$, $C_{GaN} = 3.12 \text{ MJ/m}^3\text{K}$, and interface conductance of $G_{Al-GaN} = 80 \text{ MW/m}^2\text{K}$.

Figure 8 shows our calibration measurements of the TDTR system on several standard samples including diamond, SiC, GaN, Si, and sapphire with thermal conductivity ranging from 1 W/mK to 10^3 W/mK. Our measurement agrees well with the reference values.

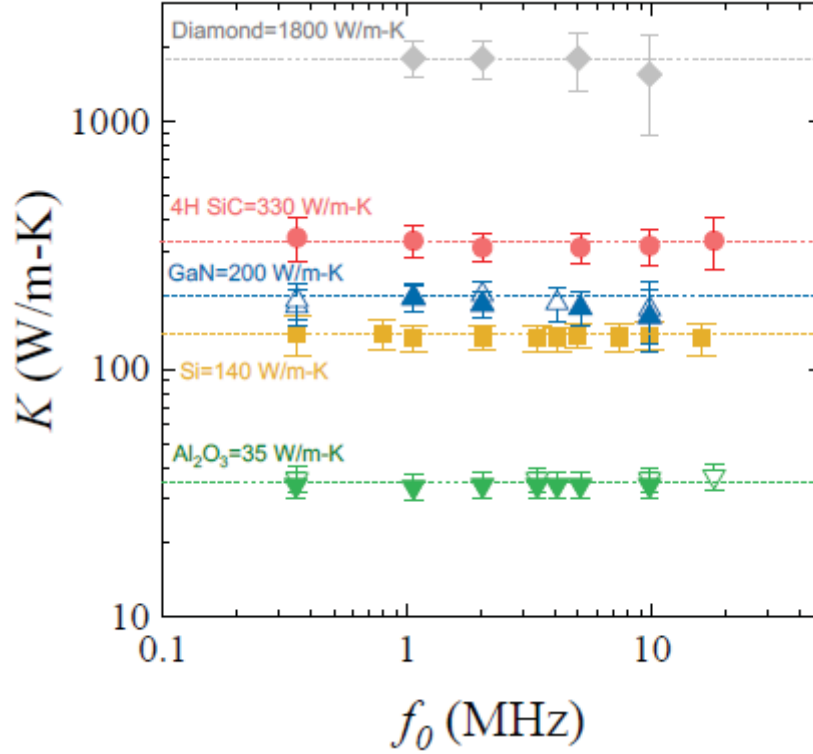


Figure 8: Calibration Measurement of our TDTR System
The dash lines are the standard reference.³²⁻³⁴

4.2 Frequency Filtering Effect of the Metal Thin Film in TDTR

In this part, we discuss the physical picture of the frequency filtering effect in TDTR. There are two major factors resulting in our prediction: i) multi-frequency heating in TDTR and ii) finite response time of the metal transducer layer.

Multi-frequency Heating in TDTR. In TDTR, the femtosecond pump laser pulses are modulated with a sinusoidal envelope (see Figure 9a). By applying Fourier transform, there exist a series of frequencies $\omega_0 \pm n\omega_s$, where ω_0 is the modulation frequency (the sinusoidal envelop of the pump beam in Figure 9b). When the aluminum transducer is subject to the multi-frequency heating, the transducer would respond differently to the heating components with different frequency. This is due to the fact that there exist a characteristic response time in the Al/Substrate system.

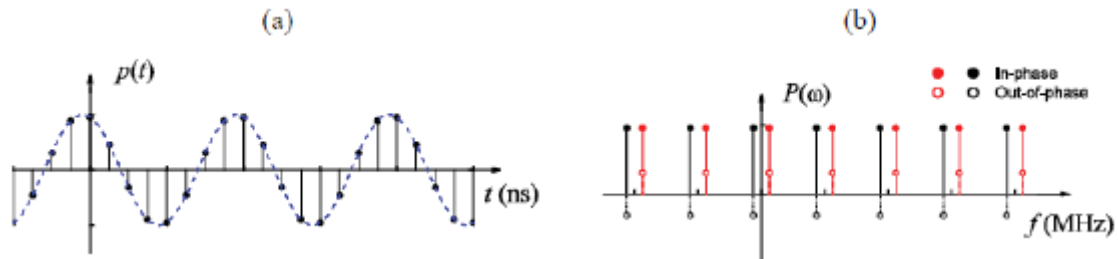


Figure 9: (a) Modulated Pump Pulses in Time Domain and (b) Pump Pulses in Frequency Domain

Response Time of the Transducer/Substrate System. Due to the existence of the aluminum transducer, it takes a certain amount of time τ_c until the substrate can follow the temperature oscillation at a certain frequency. When the periodic laser heating incident on the sample surface, the characteristic time τ_1 it takes until thermal equilibrium is reached in the aluminum transducer can be approximated by equating the penetration length $L_p = \sqrt{\frac{k_{Al}}{C_{Al}}} \tau_1$ to the aluminum thickness d_{Al} ,

$$\tau_1 = \frac{C_{Al}}{k_{Al}} d_{Al}^2 \quad (16)$$

where k_{Al} and C_{Al} is the thermal conductivity and volumetric heat capacity of aluminum transducer. After the transducer film reaches local equilibrium, the heat conduction is dominated by the interfacial heat conduction, and the temperature oscillation of the aluminum film can be described by a lumped-capacity model:

$$C_{Al} d_{Al} \frac{dT_{Al}}{dt} = G(T_{sub}(z=0) - T_{Al}) \quad (17)$$

where G is the interface conductance between the $T_{sub}(z=0)$ is the temperature at the interface on the substrate side. The characteristic time τ_2 can be obtained by non-dimensionalize equation (2):

$$\tau_2 = C_{Al} d_{Al} / G \quad (18)$$

The characteristic time τ_2 describes the timescale it takes until the substrate can follow the temperature oscillation of the aluminum transducer. Therefore, τ_1 and τ_2 combined is the characteristic time it takes until the temperature of the substrate is following the periodic laser heating.

$$\tau_c = \tau_1 + \tau_2 = \frac{C_{Al} d_{Al}^2}{k_{Al}} + \frac{C_{Al} d_{Al}}{G} \quad (19)$$

The characteristic time τ_c describes the timescale it takes until the substrate can follow the temperature oscillation of the aluminum transducer. Therefore, τ_1 and τ_2 combined is the characteristic time it takes until the temperature of the substrate is following the periodic laser heating.

Due to the characteristic time introduced by the transducer layer, the substrate can only follow the temperature oscillation with frequency $\omega_H \ll 2\pi/\tau_c$, and the temperature oscillation with frequency higher than $2\pi/\tau_c$ would be filtered by the transducer layer and the interface such that

the substrate would not respond. The physical picture is shown in Figure 10. Equation (19) demonstrates that we can selectively control the frequency range that can penetrate into the substrate by varying the thickness of the transducer layer. The thinner the transducer layer is deposited, the more high-frequency components in TDTR experiment would be allowed to penetrate into the substrate, and the lower the thermal conductivity would be measured due to the ballistic effects from high frequency components.

In conclusion, we expect that the measured apparent thermal conductivity would be a function of both aluminum thickness and the modulation frequency $k_A(\omega_0, d_{Al})$, and k_A would decrease with increasing modulation frequency ω_0 and decreasing d_{Al} .

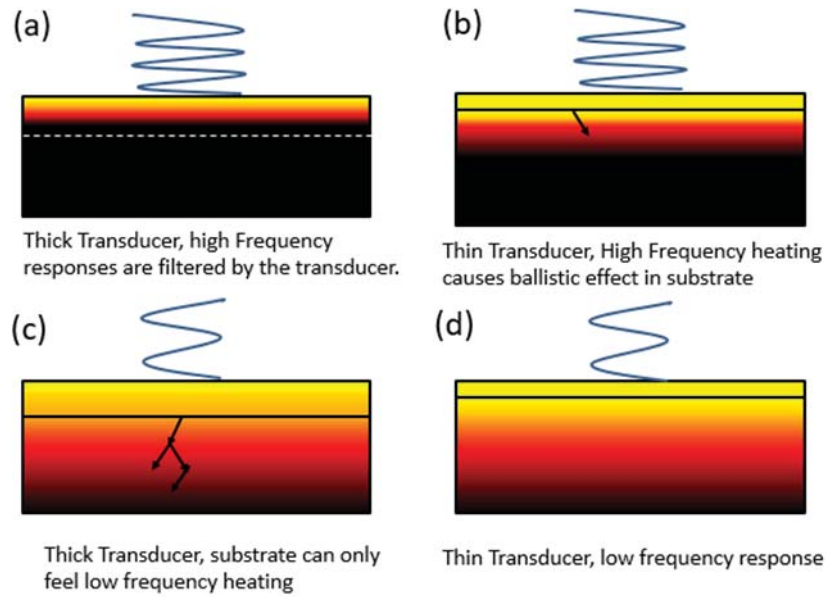


Figure 10: Physical Picture of Frequency Filtering Effect of the Transducer Layer at different Heating Frequencies

4.3 Experimental Observation of the Frequency Filtering Effect

Temperature-Dependent Thermal Conductivity of GaN. Figure 11 shows the measured thermal conductivity of GaN from 80 K to 300 K. The measured thermal conductivity decrease when the modulation frequency increases. This might be attributed to the quasi-ballistic transport when the penetration depth d_p becomes comparable with the phonon MFP in GaN. We treat these results with caution, because using an erroneous spot radius might also result in the frequency dependent thermal conductivity. To rule out this error, we performed similar thermal conductivity measurement on sapphire, which is more sensitive to the laser spot radius in TDTR experiment. As expected, the thermal conductivity of sapphire (35 W/mK) is frequency independent at room temperature, because of the much shorter MFP than GaN. However, the frequency dependence starts to emerge at cryogenic temperature. For example, the measured thermal conductivity of sapphire decreased 25% at 100 K when the modulation frequency increased from 1 MHz to 10 MHz. At lower temperature, the phonon-phonon scattering becomes weaker, thus the MFP becomes longer than that at room temperature. Therefore, the phonon

ballistic transport and frequency dependent thermal conductivity becomes more pronounced.

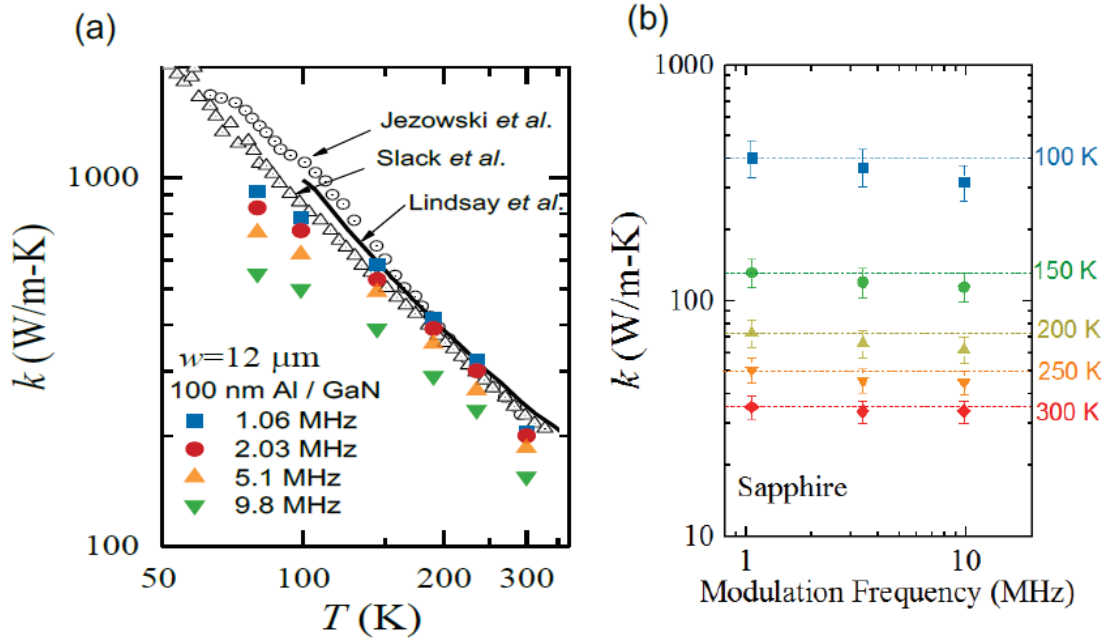


Figure 11: (a) Temperature Dependent Thermal Conductivity of GaN and (b) Frequency and Temperature Dependent Thermal Conductivity of Sapphire

The thermal conductivity is observed to decrease when higher modulation frequency is used.

Frequency-Al Thickness Dependent Thermal Conductivity of GaN. Figure 12a shows the measured thermal conductivity of GaN as a function of both modulation frequency ω_0 and the transducer thickness d_{Al} . Even at room temperature, the ballistic effect is pronounced. For each d_{Al} , the thermal conductivity of GaN decreased when the modulation frequency increases. At the same time, the thermal conductivity also decreases if thinner aluminum is deposited on top of the GaN substrate. As discussed, the thinner aluminum transducer would have a shortened response time, thereby allowing more high frequency heating components penetrating into the GaN substrate. As a result, the high frequency heating components would suppress the phonon MFPs and cause a lower measured thermal conductivity. We have also designed a control group. We measured the thermal conductivity of a series of silica samples with different Al thickness. Since silica has very low thermal conductivity ($\sim 1.4 \text{ W/mK}$) and short MFPs (tens of nanometers), we should not observe any ballistic effect at room temperature, and the thermal conductivity should be independent of ω_0 and d_{Al} .

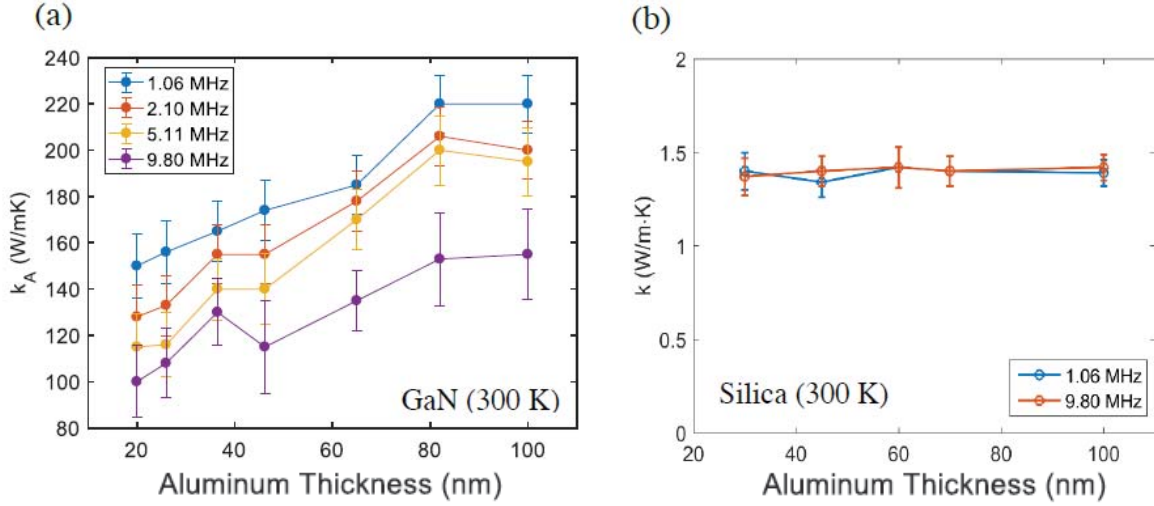


Figure 12: (a) Temperature Dependent Thermal Conductivity of GaN and (b) Frequency and Temperature Dependent Thermal Conductivity of Sapphire

The thermal conductivity is observed to decrease when higher modulation frequency is used.

We have also measured the frequency and Al thickness dependent thermal conductivity of GaN at cryogenic temperature 100 K. Interestingly, the aluminum thickness dependence is even weaker than room temperature. Thermal conductivity is decreased by only 10 % when d_{Al} is reduced from 100 nm to 20 nm, as compared to $\sim 20\%$ thermal conductivity reduction at room temperature. The reason lies in the temperature dependent thermal conductivity k_{Al} and G of the Al/GaN interface. At cryogenic temperature, both k_{Al} and G decreased, resulting in a slower response time $\tau_c = \frac{C_{Al}d_{Al}^2}{k_{Al}} + \frac{C_{Al}d_{Al}}{G}$. As a result, it becomes even harder for the high frequency heating components to penetrate into the substrate due to the stronger frequency filtering effect.

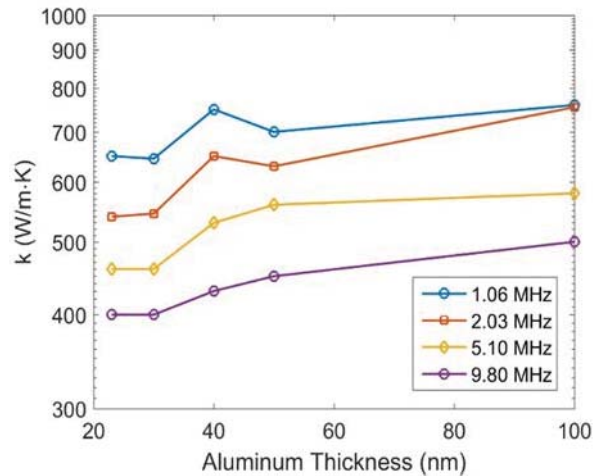


Figure 13: Aluminum Thickness Dependent and Frequency Dependent Thermal Conductivity of GaN at 100 K

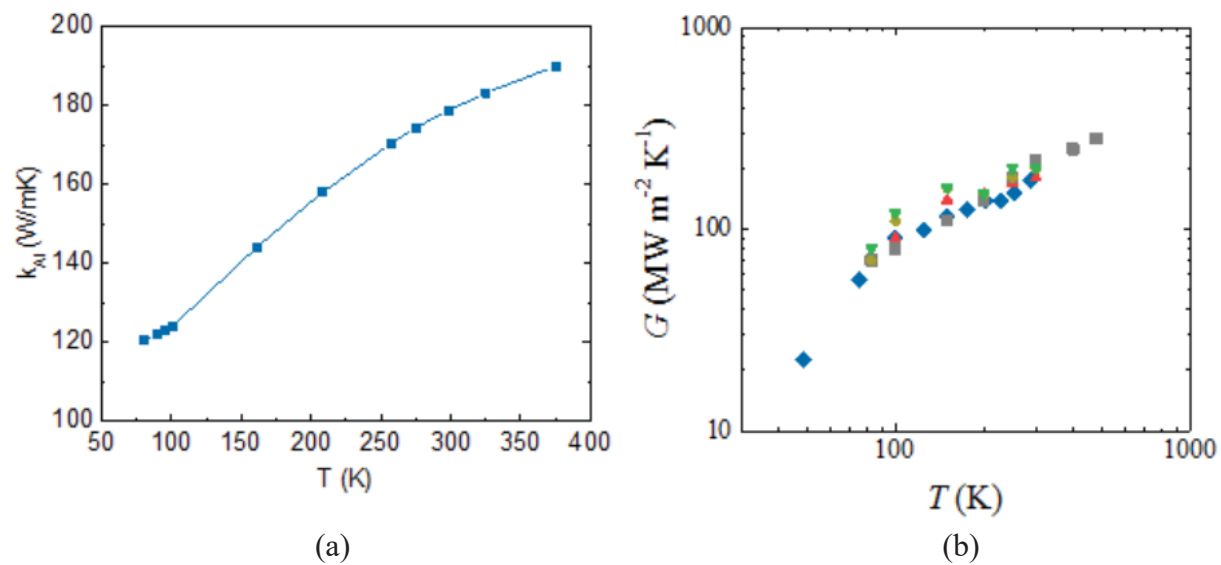


Figure 14: Temperature Dependent (a) Thermal Conductivity of Al and (b) Conductance of the Al/GaN Interface

5. SUMMARY

We have performed first-principles calculations to predict the phonon and thermal properties. The phonons with mean free paths larger than 1 μm contribute $\sim 50\%$ thermal conductivity for diamond, GaN and SiC. We have studied dependence of GaN thermal conductivity on the heater thickness and heating frequency. We found that thick heater would prevent high frequency heating from penetrating into the substrate. This research suggests that the size effect of thermal conductivity in GaN devices is collectively determined by several characteristic length scales, and the previous knowledge of size effect is too simple to understand heat dissipation in practical HEMT devices.

6. REFERENCES

1. Chen, G., *Nanoscale Energy Transport and Conversion: A Parallel Treatment of Electrons, Molecules, Phonons, and Photons*; Oxford University Press, USA, 2005.
2. Siemens, M. E.; Li, Q.; Yang, R.; Nelson, K. A.; Anderson, E. H.; Murnane, M. M.; Kapteyn, H. C., Quasi-Ballistic Thermal Transport from Nanoscale Interfaces Observed Using Ultrafast Coherent Soft X-Ray Beams. *Nat Mater* **2010**, 9, 26-30.
3. Hu, Y.; Zeng, L.; Minnich, A. J.; Dresselhaus, M. S.; Chen, G., Spectral Mapping of Thermal Conductivity through Nanoscale Ballistic Transport. *Nature nanotechnology* **2015**, 10, 701-6.
4. Regner, K. T.; Sellan, D. P.; Su, Z.; Amon, C. H.; McGaughey, A. J.; Malen, J. A., Broadband Phonon Mean Free Path Contributions to Thermal Conductivity Measured Using Frequency Domain Thermoreflectance. *Nature communications* **2013**, 4, 1640.
5. Gu, X.; Yang, R., First-Principles Prediction of Phononic Thermal Conductivity of Silicene: A Comparison with Graphene. *Journal of Applied Physics* **2015**, 117, 025102.
6. Ward, A.; Broido, D.; Stewart, D. A.; Deinzer, G., Ab Initio Theory of the Lattice Thermal Conductivity in Diamond. *Physical Review B* **2009**, 80, 125203.
7. Li, W.; Lindsay, L.; Broido, D.; Stewart, D. A.; Mingo, N., Thermal Conductivity of Bulk and Nanowire Mg₂Si_{1-x}Sn_x Alloys from First Principles. *Physical Review B* **2012**, 86, 174307.
8. Esfarjani, K.; Chen, G.; Stokes, H. T., Heat Transport in Silicon from First-Principles Calculations. *Physical Review B* **2011**, 84, 085204.
9. Asen-Palmer, M.; Bartkowski, K.; Gmelin, E.; Cardona, M.; Zhernov, A.; Inyushkin, A.; Taldenkov, A.; Ozhogin, V.; Itoh, K.; Haller, E., Thermal Conductivity of Germanium Crystals with Different Isotopic Compositions. *Physical review B* **1997**, 56, 9431.
10. Li, W.; Mingo, N.; Lindsay, L.; Broido, D.; Stewart, D. A.; Katcho, N., Thermal Conductivity of Diamond Nanowires from First Principles. *Physical Review B* **2012**, 85, 195436.
11. Van der Vorst, H. A., Bi-Cgstab: A Fast and Smoothly Converging Variant of Bi-Cg for the Solution of Nonsymmetric Linear Systems. *SIAM Journal on scientific and Statistical Computing* **1992**, 13, 631-644.
12. Giannozzi, P., et al., Quantum Espresso: A Modular and Open-Source Software Project for Quantum Simulations of Materials. *J. Phys.: Condens. Matter* **2009**, 21, 395502.
13. Holloway, H.; Hass, K.; Tamor, M.; Anthony, T.; Banholzer, W., Isotopic Dependence of the Lattice Constant of Diamond. *Physical Review B* **1991**, 44, 7123.
14. Levinshstein, M. E.; Rumyantsev, S. L.; Shur, M. S., *Properties of Advanced Semiconductor Materials: GaN, AlN, InN, BN, SiC, SiGe*; John Wiley & Sons, 2001.
15. Schulz, H.; Thiemann, K., Crystal Structure Refinement of AlN and GaN. *Solid State Communications* **1977**, 23, 815-819.
16. Baroni, S.; De Gironcoli, S.; Dal Corso, A.; Giannozzi, P., Phonons and Related Crystal Properties from Density-Functional Perturbation Theory. *Reviews of Modern Physics* **2001**, 73, 515.
17. Tang, X.; Fultz, B., First-Principles Study of Phonon Linewidths in Noble Metals. *Physical Review B* **2011**, 84, 054303.

18. Lindsay, L.; Broido, D.; Reinecke, T., Ab Initio Thermal Transport in Compound Semiconductors. *Physical Review B* **2013**, *87*, 165201.
19. Warren, J.; Yarnell, J.; Dolling, G.; Cowley, R., Lattice Dynamics of Diamond. *Physical Review* **1967**, *158*, 805.
20. Feldman, D.; Parker Jr, J. H.; Choyke, W.; Patrick, L., Phonon Dispersion Curves by Raman Scattering in Sic, Polytypes 3 C, 4 H, 6 H, 1 5 R, and 2 1 R. *Physical Review* **1968**, *173*, 787.
21. Ruf, T.; Serrano, J.; Cardona, M.; Pavone, P.; Pabst, M.; Krisch, M.; D'astuto, M.; Suski, T.; Grzegory, I.; Leszczynski, M., Phonon Dispersion Curves in Wurtzite-Structure Gan Determined by Inelastic X-Ray Scattering. *Physical review letters* **2001**, *86*, 906.
22. Fugallo, G.; Lazzeri, M.; Paulatto, L.; Mauri, F., Ab Initio Variational Approach for Evaluating Lattice Thermal Conductivity. *Physical Review B* **2013**, *88*, 045430.
23. Wei, L.; Kuo, P.; Thomas, R.; Anthony, T.; Banholzer, W., Thermal Conductivity of Isotopically Modified Single Crystal Diamond. *Physical Review Letters* **1993**, *70*, 3764.
24. Berman, R.; Hudson, P.; Martinez, M., Nitrogen in Diamond: Evidence from Thermal Conductivity. *Journal of Physics C: Solid State Physics* **1975**, *8*, L430.
25. Slack, G. A.; Schowalter, L. J.; Morelli, D.; Freitas, J. A., Some Effects of Oxygen Impurities on Aln and Gan. *Journal of Crystal Growth* **2002**, *246*, 287-298.
26. Jeżowski, A.; Stachowiak, P.; Plackowski, T.; Suski, T.; Krukowski, S.; Boćkowski, M.; Grzegory, I.; Danilchenko, B.; Paszkiewicz, T., Thermal Conductivity of Gan Crystals Grown by High Pressure Method. *physica status solidi(b)* **2003**, *240*, 447-450.
27. Wei, R.; Song, S.; Yang, K.; Cui, Y.; Peng, Y.; Chen, X.; Hu, X.; Xu, X., Thermal Conductivity of 4h-Sic Single Crystals. *Journal of Applied Physics* **2013**, *113*, 053503.
28. Ziade, E.; Yang, J.; Brummer, G.; Nothorn, D.; Moustakas, T.; Schmidt, A. J., Thickness Dependent Thermal Conductivity of Gallium Nitride. *Appl. Phys. Lett.* **2017**, *110*, 031903.
29. Minnich, A. J.; Johnson, J. A.; Schmidt, A. J.; Esfarjani, K.; Dresselhaus, M. S.; Nelson, K. A.; Chen, G., Thermal Conductivity Spectroscopy Technique to Measure Phonon Mean Free Paths. *Phys. Rev. Lett.* **2011**, *107*, 095901.
30. Koh, Y. K.; Cahill, D. G., Frequency Dependence of the Thermal Conductivity of Semiconductor Alloys. *Phys. Rev. B* **2007**, *76*.
31. Malen, J. A.; Baheti, K.; Tong, T.; Zhao, Y.; Hudgings, J. A.; Majumdar, A., Optical Measurement of Thermal Conductivity Using Fiber Aligned Frequency Domain Thermoreflectance. *J. Heat Transfer* **2011**, *133*, 081601.
32. Schmidt, A. J., Pump-Probe Thermoreflectance. *Annual Review of Heat Transfer* **2013**, *16*.
33. Zhu, J.; Tang, D.; Wang, W.; Liu, J.; Holub, K. W.; Yang, R., Ultrafast Thermoreflectance Techniques for Measuring Thermal Conductivity and Interface Thermal Conductance of Thin Films. *J. Appl. Phys.* **2010**, *108*, 094315.
34. Liu, J.; Zhu, J.; Tian, M.; Gu, X.; Schmidt, A.; Yang, R., Simultaneous Measurement of Thermal Conductivity and Heat Capacity of Bulk and Thin Film Materials Using Frequency- Dependent Transient Thermoreflectance Method. *Rev. Sci. Instrum.* **2013**, *84*, 034902.

LIST OF ABBREVIATIONS, ACRONYMS, AND SYMBOLS

ACRONYM	DESCRIPTION
BTE	Boltzman transport equation
CVD	chemical-vapor-deposited
DARPA	Defense Advanced Research Projects Agency
DFPT	density-functional perturbation theory
DFT	density functional theory
EOM	electro-optic modulator
GaN	gallium nitride
HEMT	high electron mobility transistor
MFP	mean free path
MTO	Microsystems Technology Office
PBTE	Peierls-Boltzmann Transport Equation
SiC	silicon carbide
TDTR	time-domain thermoreflectance